



Holey wrinkled-multilayered graphene scaffolds for uniform Li-ion flux enabling high-performance lithium metal anodes

Sangyeop Kim ^a, Incheol Heo ^a, Jun Hyuk Kang ^{b,c}, Min Seok Kang ^a, Junsung Lee ^a, Hee Soo Kim ^d, Dong-Ha Lim ^d, Sung Beom Cho ^{b,c,e}, Won Cheol Yoo ^{a,f,*}

^a Department of Applied Chemistry, Center for Bionano Intelligence Education and Research, Hanyang University, ERICA, Ansan 15588, Republic of Korea

^b Department of Energy Systems Research, Ajou University, Suwon 16499, Republic of Korea

^c Department of Materials Science and Engineering, Ajou University, Suwon 16499, Republic of Korea

^d Low Carbon Energy Group, Korea Institute of Industrial Technology (KITECH), Ulsan 44413, Republic of Korea

^e Ajou Energy Science Research Center, Ajou University, Suwon 16499, Republic of Korea

^f Department of Energy and Bio Sciences, Hanyang University, ERICA, Ansan 15588, Republic of Korea

ARTICLE INFO

Article history:

Received 7 August 2025

Revised 14 September 2025

Accepted 15 September 2025

Available online 24 September 2025

Keywords:

Binder-free electrode

Holey wrinkled-multilayered graphene

Tortuosity

Lithium metal anode

Host design

ABSTRACT

The practical use of lithium metal anodes (LMAs) is impeded by uncontrolled dendrite growth, primarily caused by uneven Li-ion flux and significant volume changes during cycling. To overcome these challenges, we present binder-free holey wrinkled-multilayered graphene (HWMG) scaffolds for high-performance LMAs with long cycle life. Holey graphene oxide (HGO) sheets were restacked into particle-like holey wrinkled-multilayered graphene oxide (HWMGO) in a high-concentration GO suspension, in which few-layer HGOs were quickly stabilized and wrinkled during the drying process, and upon reduction, they transformed into HWMG. HWMG exhibited excellent adhesion due to chemical interactions via edge-located functional groups. Its particle-like morphology, with numerous nanopores and high porosity, conferred outstanding mechanical flexibility and low tortuosity, enabling uniform Li-ion flux, buffering volume expansion, and suppressing dendrite growth. As a result, excellent long-term stability over 800 cycles and a voltage hysteresis of ca. 7 mV over 6000 h were realized for the HWMG scaffolds, and a high areal capacity of 3.34 mAh cm^{-2} at 0.3 C after 350 cycles was demonstrated in a full-cell configuration. This work promotes the practical application of LMAs by offering a scalable scaffold design that suppresses dendrites and enhances cycle life.

© 2025 Science Press and Dalian Institute of Chemical Physics, Chinese Academy of Sciences. Published by Elsevier B.V. and Science Press. All rights are reserved, including those for text and data mining, AI training, and similar technologies.

1. Introduction

With the rapid development of modern society, there is an increasing demand for high-energy-density secondary batteries, which are essential for electric vehicles and portable electronic devices [1,2]. In this regard, lithium metal anodes (LMAs), with a high theoretical capacity (3860 mAh g^{-1}) and a low reduction potential (-3.04 V vs. standard hydrogen electrode), are promising candidates for high-energy-density lithium-ion batteries (LIBs) [3–5]. However, the high chemical reactivity of lithium and its significant volume changes during plating and stripping hinder

the practical use of LMAs. These effects lead to uncontrolled dendrite growth, low coulombic efficiency (CE), rapid capacity fading, increased voltage hysteresis, and an elevated risk of short circuits, thereby delaying commercialization [1,6,7].

Interfacial engineering and host design have been widely employed to address the challenges faced by LMAs. Stable interphases on Li metal have been generated by designing electrolytes, additives [8–10], polymers [11,12], LiF [13,14], solid electrolytes [15,16], and diamond films [17,18] that exhibit chemical and mechanical stability to manage dendrite growth during prolonged cycling [19]. Additionally, host design is an effective approach to simultaneously mitigate significant volume changes and suppress dendrite growth [20–22]. Host candidates possess several important features such as electrical conductivity, lithiophilic surfaces, porous nature, chemical stability, mechanical

* Corresponding author.

E-mail address: wcyoo@hanyang.ac.kr (W.C. Yoo).

strength, and flexibility [23–25]. Three-dimensional (3D) metallic scaffolds have been proposed [26,27]; however, their high density and limited synthetic methods have hampered their practical application [24]. In this regard, carbonaceous materials, including 3D carbon [28,29], hollow carbon spheres [30], and heteroatom-doped carbon [31,32], can be considered promising scaffolds that buffer volume changes and suppress undesirable dendrite growth. In particular, reduced graphene oxide (rGO) has shown promising results because it exhibits high electrical conductivity and good lithiophilicity without additional lithiophilic coating or heteroatom doping, owing to the intrinsic oxygen-containing functional groups on the surface [25,33,34]. Moreover, rGO exhibits outstanding mechanical strength and flexibility, which can mitigate volume changes during the plating and stripping processes [35–37].

Among the aforementioned features of host materials for LMAs, the tortuosity of scaffolds has recently attracted significant attention [38–40]. It is important that a facile Li-ion flux down to the lower part of the electrode is desired; otherwise, Li preferentially accumulates in the upper part of the host, resulting in insufficient use of the lower part of the scaffold and an uneven current distribution, thus reducing the anode life. Cui et al. successfully demonstrated the effect of tortuosity for LMAs: a low-tortuosity electrode (vertically aligned rGO aerogel) exhibited excellent cycling stability compared with its counterparts (laterally and randomly aligned rGO aerogels) because of the homogeneous Li-ion flux, resulting in uniform Li deposition across the host [23]. In this regard, the requisites for a successful LMA host include a lithiophilic surface, electrical conductivity, mechanical flexibility, chemical stability, and low tortuosity; however, candidate hosts with the aforementioned characteristics are still limited.

Herein, we report holey wrinkled-multilayered graphene (HWMG) as a binder-free host material for high-performance LMAs. Holey graphene oxide (HGOs) were restacked to form HWMG oxide (HWMGO) in a high-concentration (ca. 9 wt%) GO suspension because few-layer HGOs were quickly stabilized and restacked into relatively stable GO segments [41], which readily wrinkled or crumpled during the drying process. HWMGO was directly deposited on a Cu current collector without a binder owing to its excellent adhesion, arising from chemical interactions via edge-located functional groups, and was then thermally reduced to form HWMG. In addition, HWMG showed outstanding mechanical flexibility and low tortuosity owing to wrinkled and particle-like morphology with numerous nanopores and high porosity. To highlight the advantages of HWMG, we also prepared nonporous wrinkled-multilayered graphene (WMG) and conventional film-like multilayered graphene (MG) for comparison.

The electrochemical performance of HWMG, WMG, WMG with polyvinylidene fluoride (PVDF) binders of various contents, and MG films was tested to elucidate the influence of the binder effect and morphological features on electrode tortuosity and electrochemical behavior. The binder-free HWMG hosts exhibited superior electrochemical performance with an average CE of 98.9 % over 800 cycles in the asymmetric cell test and a low voltage hysteresis of approximately 7 mV for 6000 h in the symmetric cell test, as compared to the counterparts. Furthermore, in the full-cell configuration with lithium iron phosphate (Li@HWMG||LFP), 71.6 % capacity retention compared to the 3rd cycle after 500 cycles (30.7 mg cm^{-2} , theoretical capacity of 4.39 mAh cm^{-2}), and 85.6 % capacity retention (3.34 mAh cm^{-2}) compared to the 3rd cycle after 350 cycles at a higher cathode mass loading (36.8 mg cm^{-2} , theoretical capacity of 5.01 mAh cm^{-2}) were achieved. Therefore, the binder-free HWMG with outstanding mechanical flexibility and low tortuosity enabled the homogeneous Li-ion flux across the electrode and uniform Li plating during repeated cycles, result-

ing in excellent long-term stability applicable to practical cell configurations.

2. Results and discussion

2.1. Fabrication and characterization of hosts

To facilitate Li-ion transport, holey GO sheets prepared by a mild defect-etching reaction using a diluted hydrogen peroxide (H_2O_2) solution were employed to prepare HWMG (Fig. 1a). The size of nanopores was controlled by varying the reaction times (2, 4, 6, 8, and 16 h), denoted as HGO_2, 4, 6, 8, and 16h. Transmission electron microscopy (TEM) images demonstrated that while HGO_2h did not show any nanopores, HGO_4h began to exhibit small etching defects around 1–2 nm in size, which further expanded to 2–3 nm in HGO_6h (Fig. S1). Upon prolonged reaction times, HGO_8h and HGO_16h exhibited nanopores of ca. 5 and >10 nm, respectively (Fig. 1b, c). Subsequently, HGOs with distinct nanopores (i.e., HGO_8h and HGO_16h) were used to synthesize HWMGOs (hereafter denoted as HWMGO_8h and HWMGO_16h) by a simple drying process using a high-concentration (ca. 9 wt %) HGO suspension, based on a previous report (Fig. 1a) [41]. Meanwhile, nonporous wrinkled-multilayered graphene oxide (WMGO) and multilayered GO (MGO) were synthesized by a simple drying process with high (9 wt%) and low (0.5 wt%) concentration GO suspensions, respectively (Fig. S2) [41]. X-ray diffraction (XRD) peaks with different intensities at ca. 11° , corresponding to the d -spacing of restacked GO sheets, were identified for MGO, WMGO, and HWMGO_8h. MGO showed a much sharper peak than WMGO and HWMGO_8h, which had similar peak intensities (Fig. 1d), suggesting that the degrees of restacking for HWMGO_8h and WMGO were similar and much lower than those of MGO. On the other hand, the peak intensity of HWMGO_16h was significantly lower than the others (Fig. 1d), confirming the insufficient degree of restacking of HWMGO_16h due to more defects in the basal plane that prevented efficient π - π restacking (Fig. 1d and Fig. S3).

TEM images showed that MGO had much thicker multilayers (ca. 20 nm) than those for WMGO and HWMGO_8h (ca. 6 nm) (Fig. 1e, f, and Fig. S4). The multilayer thicknesses were additionally estimated from XRD analysis using the Debye-Scherrer equation, yielding values of approximately 17.7 nm for MGO and 7.1 nm for both WMGO and HWMGO_8h, which are consistent with the TEM observations. This was also supported by Raman spectroscopy, which showed higher disordered (D) and graphite (G) band intensities for MGO compared with WMGO and HWMGO_8h. Furthermore, when comparing with WMGO, HWMGO_8h had relatively lower both bands and showed a higher D/G ratio, indicating the presence of defect sites (Fig. S5). According to scanning electron microscopy (SEM) images of the samples, HWMGO_8h and WMGO exhibited a particle-like morphology with wrinkled surfaces, whereas MGO exhibited featureless morphology (Fig. 1g and Fig. S6), attributable to the thinner multilayer thicknesses for WMGO and HWMGO_8h samples, which readily wrinkle during the drying process. The average width of GO sheets, estimated from SEM images of the parent graphite and low-magnification TEM images of MGO, ranged from approximately 7.5 to 14.0 μm (Fig. S7).

To investigate the chemical properties, X-ray photoelectron spectroscopy (XPS) and elemental analysis (EA) were conducted on WMGO, HWMGO_8h, and HWMGO_16h (Fig. S8 and Table S1). The EA results showed a decrease in the oxygen content as the reaction time increased (36.1 %, 33.4 %, and 30.5 %, respectively) (Table S1). This decrease is attributed to the nanopore-formation mechanism, whereby oxygen defect sites are created

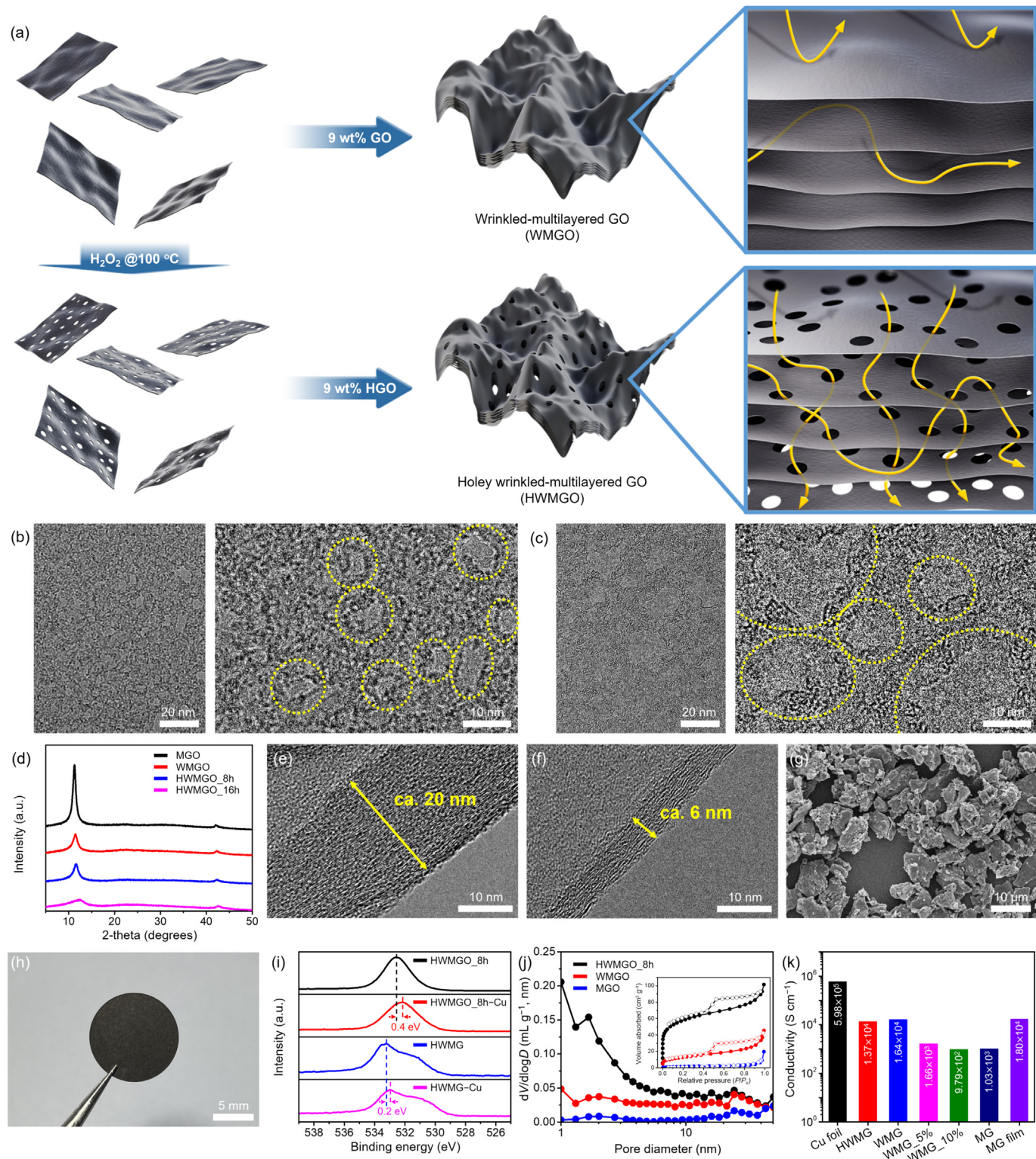


Fig. 1. Material characterizations of hosts with different morphologies. Schematic illustration for HWMGO and WMGO formation (a). TEM images of HGO_{8h} (b) and HGO_{16h} (c). XRD patterns of MGO, WMGO, HWMGO_{8h}, and HWMGO_{16h} (d). TEM images of MGO (e) and HWMGO_{8h} (f). SEM image of HWMGO_{8h} (g). Photograph of the HWMGO electrode without the binder (h). XPS results for O 1s of HWMGO, HWMGO-Cu, HWMG, and HWMG-Cu (i). BJH profiles of HWMGO, WMGO, and MGO (j). Inset in (j): nitrogen sorption isotherms of HWMGO, WMGO, and MGO. Electrical conductivity results of various electrodes measured using the 4-probe technique (k).

on the GO surface during oxidation and are subsequently etched out with prolonged reaction time [42,43]. The oxygen percentages for MGO and WMGO were nearly identical, while HWMGO_{8h} exhibited a slightly lower oxygen percentage (Table S1). After ther-

mal reduction, XPS analysis confirmed that the O 1s peaks were similar for MG, WMG, and HWMG_{8h} (Fig. S9 and Table S1). The EA results showed that the oxygen percentages were 13.4 %, 13.3 %, and 13.3 % for MG, WMG, and HWMG_{8h}, respectively,

confirming relatively high and similar oxygen contents on the graphene surfaces (Table S1). It is well known that rGO surfaces with intrinsic oxygen content exhibit lithiophilic properties [24,31,37].

The HWMGO_8h and WMGO were then slurry-cast on a Cu current collector without a binder and subsequently subjected to thermal reduction at 300 °C to produce HWMG_8h (hereafter denoted as HWMG) and WMG. Even after thermal reduction, the HWMG and WMG films remained stably attached to both the Cu surface and between individual HWMG and WMG particles (Fig. 1h and Fig. S10a). To elucidate the adhesion property of HWMGO_8h and WMGO to the Cu surface, we used the composites consisting of HWMGO_8h and WMGO with Cu microparticles (HWMGO_8h-Cu and WMGO-Cu) for characterization purposes because the large number of interfaces between Cu and HWMGO_8h and WMGO readily enabled Fourier-transform infrared spectroscopy (FT-IR) and XPS characterization. According to FT-IR and XPS measurements for HWMGO_8h and HWMGO_8h-Cu, the C-O and O 1s peak positions of the HWMGO_8h-Cu composite were slightly shifted to lower wavenumber by up to 17 cm⁻¹ and lower binding energy by 0.4 eV, respectively, compared to HWMGO_8h (Fig. 1i and Fig. S11a), which were attributed to the coordinative interaction between oxygen and Cu [44–46]. Similar phenomena occurred for WMGO-Cu that C-O and O 1s peak positions of the WMGO-Cu composite were slightly shifted to lower wavenumber by up to 25 cm⁻¹ and lower binding energy by 0.5 eV, respectively, compared to WMGO (Fig. S11b, c).

Additionally, shifts of 0.2 and 0.3 eV were observed for HWMG-Cu and WMG-Cu, respectively, compared with HWMG and WMG (Fig. 1i and Fig. S11c). To explore the interactions between HWMGO_8h and WMGO particles, FT-IR analysis was applied to two different HWMGO and WMGO states: powdery HWMGO_8h and WMGO, and roll-pressed HWMGO_8h and WMGO (the detailed synthetic processes are included in the Supporting Information). The O-H stretching shifted from 3193 and 3174 cm⁻¹ in the powdery HWMGO_8h and WMGO to 3129 and 3094 cm⁻¹ in the roll-pressed HWMGO_8h and WMGO, resulting in a red shift of 64 and 80 cm⁻¹, respectively (Fig. S12) [47]. These shifts were attributed to the increased hydrogen bonding interactions between the roll-pressed HWMGO_8h and WMGO particles [48]. These observations confirmed the excellent adhesion of the binder-free HWMG and WMG electrodes.

In contrast, the MGO film without a binder was readily peeled from the current collector (Fig. S10b). FT-IR measurements also showed no peak shifts for the oxygen functional groups in the MGO and MGO-Cu particle composites (Fig. S13). When considering the similar chemical features of the HWMGO_8h, WMGO, and MGO samples, such different adhesion properties could be ascribed to their morphological features. It is generally accepted that oxygen moieties are preferred at the edge sites rather than at the basal plane of the GO sheets [25,49]; therefore, HWMGO_8h and WMGO have more interfacial interactions between the edge-located functional groups of GO and the Cu surface because of their particle-like and wrinkled features. In contrast, MGO preferentially interacted with the Cu surface through its basal plane because of its film-like nature. Consequently, the MG electrode was fabricated with a 10 wt% PVDF binder.

Nitrogen adsorption isotherm measurements were performed on the samples, in which much higher nitrogen uptake at very low relative pressure was identified for HWMGO_8h compared with WMGO and MGO samples (actually WMGO had a slightly higher uptake than MGO). The specific surface areas (SSAs) and total pore volumes of HWMGO_8h, WMGO, and MGO were 211.6, 47.2, and 6.7 m² g⁻¹, and 0.157, 0.069, and 0.030 cc g⁻¹, respectively (Fig. 1j and Table S2). Corresponding pore size distribution (PSD) profiles obtained by the Barrett-Joyner-Halenda (BJH) method for HWMGO_8h, WMGO, and MGO were shown in

Fig. 1(j), in which largely developed PSD below 10 nm was clearly identified for HWMGO_8h rather than the other samples. It could be concluded that the highly developed mesopores of less than 10 nm in the HWMGO_8h sample were attributed to the presence of nanopores on the basal plane of GO in the adjuvant with particle-like morphological features, which resulted in a more porous feature for the WMGO than MGO. After thermal reduction, the porosity of the samples was well preserved: HWMG, WMG, and MG showed SSAs and total pore volumes of 231.1, 50.9, and 9.6 m² g⁻¹, and 0.252, 0.108, and 0.041 cc g⁻¹, respectively (Fig. S14 and Table S2).

The effect of the binder on the electrical conductivity of the electrodes has rarely been reported; therefore, the four-probe method was employed to measure binder-free HWMG and WMG, and WMG with various binder contents and MG electrodes. First, the electrical conductivities of binder-free HWMG, WMG, and MG films were measured, showing values of 1.37×10⁴, 1.64×10⁴, and 1.80×10⁴ S cm⁻¹, respectively (Fig. 1k and Table S3). The slightly lower conductivity of HWMG compared with WMG can be attributed to the presence of nanopores. In contrast, the electrical conductivity of the MG electrode (10 wt% PVDF) significantly decreased to 1.03×10³ S cm⁻¹. In addition, the electrical conductivities of WMG with different PVDF contents (WMG_5% and WMG_10%) were measured to be 1.66×10³ and 9.79×10² S cm⁻¹, respectively, clearly confirming that the insulating PVDF significantly decreased the electrical conductivity of the electrodes.

Meanwhile, the important feature of a Li-metal host is its flexibility, which accommodates significant volume changes during multiple plating and stripping processes. The elastic modulus (*E*) values of the HWMG, WMG, WMG_10%, and MG electrodes were measured using nanoindentation tests, which were 82.9, 110.7, 183.2, and 1322.8 MPa, respectively (Fig. S15 and Table S4). These results clearly indicated that particle-like wrinkled HWMG and WMG samples are more mechanically flexible than film-like thick MG. In addition, a negative binder effect on flexibility was identified when comparing WMG and WMG_10%. Therefore, it can be concluded that HWMG, WMG, and MG have similar chemical features but different morphological and porous features, resulting in significant differences in adhesion and electrical conductivity in electrode configurations.

2.2. Tortuosity measurements

The Li-ion flux throughout the electrode can be substantially affected by the electrode tortuosity, which is a diffusional parameter for the mass transport of the electrolyte within the electrode [38–40,50]. Because tortuosity is determined by the geometric features of the electrodes (hosts), most studies have focused on developing a low-tortuosity electrode that enables uniform Li-ion flux down to the bottom of the electrode. In this regard, the effects of electrode morphology, polymeric binder, and electrode thickness on the tortuosity of the electrode have been overlooked. In this study, we measured the tortuosity of morphologically different HWMG, WMG, and MG hosts and investigated how the morphology, binder content, and electrode thickness influenced the tortuosity of the electrodes (Fig. 2a).

We measured the tortuosity values of HWMG, WMG, MG, WMG with different PVDF binder contents (WMG_5% and WMG_10%), and twice-thicker WMG (approximately 60 μm, denoted as WMG_×2). We used the blocking-electrolyte method to measure the tortuosity, employing an electrolyte that is incapable of electrochemical reactions with the electrode within the operating potential range. The tortuosity (τ) is given by the following Eq. (1).

$$\tau = \frac{R_{\text{ion}} \times S \times k_{\text{int}} \times \varepsilon}{2d} \quad (1)$$

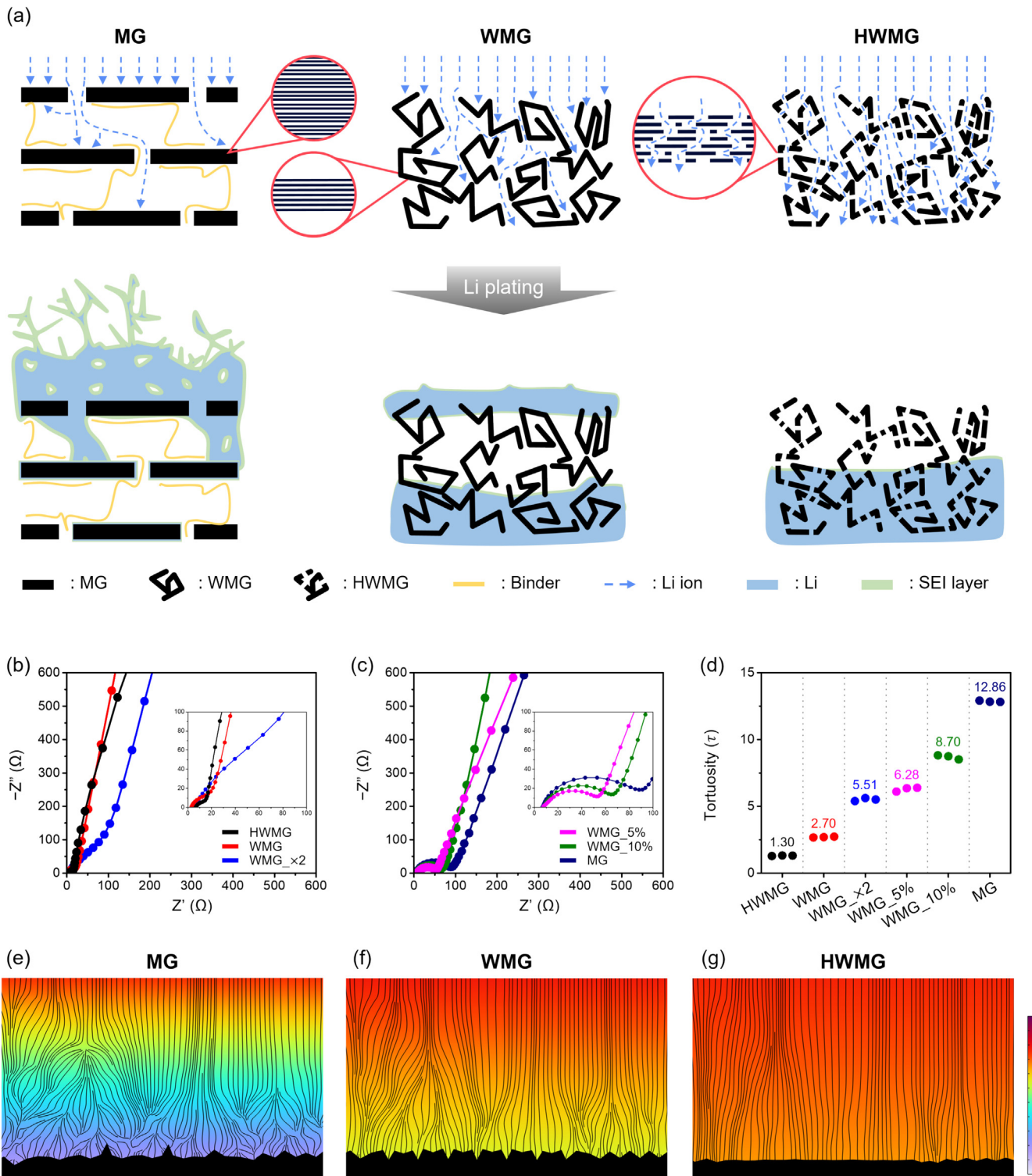


Fig. 2. Tortuosity of electrodes. Schematic illustration for tortuosity and binder effect in MG, WMG, and HWMG electrodes (a). EIS results for tortuosity calculation for binder-free HWMG, WMG, and WMG_{x2} (b) and binder-contained WMG_5%, WMG_10%, and MG electrodes (c). Inset in (b and c): enlarged EIS results, respectively. Tortuosity of various electrodes measured three times using the blocking-electrolyte method, with values shown as averages (d). Simulated Li-ion transport distribution and deposition behavior influenced by scaffold tortuosity of MG (e), WMG (f), and HWMG (g). Streamlines indicate Li-ion flux, background color represents Li-ion concentration, and the black region shows deposited Li morphology.

where R_{ion} is the effective ionic resistance in a symmetric cell configuration, S is the cross-sectional area of the cell (0.95 cm^2 in this study), k_{int} is the intrinsic conductivity of the electrolyte (0.46 mS cm^{-1} at 10 mM), ε is the porosity of the electrode, and d is the thickness of the sample. R_{ion} , the difference between the low-frequency intercept (R_l) and the high-frequency intercept

(R_h), can be obtained from electrochemical impedance spectroscopy (EIS) analysis [50–53]. The Nyquist plots of the samples are displayed in Fig. 2(b, c).

We measured the tortuosity three times per electrode, and the average tortuosity values for HWMG, WMG, WMG_5%, and WMG_10% were 1.30, 2.70, 6.28, and 8.70, respectively. First,

HWMG showed a lower tortuosity than WMG owing to numerous nanopores, resulting in higher SSA and pore volume with well-developed small mesopores. The tortuosity increased with increasing binder content (Fig. 2d and Table S5), clearly demonstrating the negative effect of a binder electrode tortuosity. In addition, the MG electrode exhibited an average tortuosity of 12.86, which was approximately ten times higher than that of the HWMG electrode and even higher than that of the WMG_10% electrode (Fig. 2d and Table S5). The high tortuosity of MG is attributed to the use of a binder and its multilayered, film-like morphology. Meanwhile, WMG_x2 exhibited a higher tortuosity of 5.51 compared to the WMG electrode (2.70), strongly suggesting the importance of an optimal electrode thickness (Fig. 2d and Table S5). Therefore, the ideal electrode configuration for uniform Li-ion flux appears to be a porous and binder-free electrode with an optimal thickness.

To investigate how scaffold tortuosity influences Li-ion flux distribution during cycling, finite element method (FEM) simulations were performed. The experimentally measured tortuosity, porosity, and electrical conductivity for the MG, WMG, and HWMG electrodes were used as input parameters (Table S6). Fig. 2(e and f) illustrates the simulated Li-ion concentration (background color) and Li-ion flux (streamlines) within these structures, with the resulting lithium deposition morphology shown in black at the base of each panel. The MG electrode, characterized by its significantly higher tortuosity, induces a highly inhomogeneous Li-ion flux. This inhomogeneity creates a starkly non-uniform Li-ion concentration with severe concentration gradients, as depicted in Fig. 2(e). For the WMG electrode, a comparatively lower yet still elevated tortuosity results in non-uniform Li-ion transport and a less uniform Li-ion concentration. This initiates irregular lithium growth, as shown in Fig. 2(f) for the WMG electrode. In contrast, the HWMG electrode, distinguished by its remarkably low tortuosity, facilitates homogeneous Li-ion transport. This leads to a uniform Li-ion concentration profile across the electrode, resulting in uniform lithium deposition (Fig. 2g). These simulation results underscore the critical role of host material tortuosity in governing Li-ion flux and suppressing dendrite formation.

2.3. Electrochemical performances

To assess the electrochemical performance of the HWMG, WMG, WMG_5%, WMG_10%, MG, and Cu foil for LMAs, CE cycling tests of asymmetric half-cells (e.g., HWMG||Li) were conducted. These tests determined the reversibility of galvanostatic Li plating/stripping at various current densities and capacities using a Li metal foil as the counter electrode. All cells underwent a stabilization process consisting of three cycles at a current density of 0.25 mA cm⁻² within a voltage range of 0–3 V. The HWMG electrode exhibited stable performance for over 800 cycles, with an average CE of 98.9 % for cycles 1–200 and 99.0 % for cycles 201–800 at a current density of 0.5 mA cm⁻² and capacity of 1.0 mAh cm⁻². In contrast, the WMG, WMG_10%, and MG electrodes showed a rapid decrease in CE after 700, 500, and 400 cycles, respectively, whereas the Cu foil exhibited a much faster CE decrease after 100 cycles (Fig. 3a). In addition, at a current density of 2.0 mA cm⁻² and a capacity of 4.0 mAh cm⁻², the HWMG electrode maintained an average CE of 98.8 % over 250 cycles (Fig. 3b). The WMG electrode, despite being binder-free, exhibited a decline in CE after 200 cycles, indicating inferior long-term stability (Fig. 3b). Furthermore, the WMG_5% electrode initially showed unstable performance, followed by a decline in CE after 100 cycles (Fig. S16), and the WMG_10% electrode exhibited an even more rapid CE drop before 100 cycles (Fig. 3b), demonstrating a clear correlation between increased binder content and unstable performance in asymmetric cell tests. Additionally, both the MG electrode and Cu foil showed a rapid decrease in CE after 55 and 10

cycles, respectively (Fig. 3b). When comparing with WMG_10% and MG electrodes that have the same binder content but different scaffold morphologies, scaffold morphology is strongly related to Li-ion flux, thereby affecting the electrochemical performance.

The pronounced contrast among HWMG, WMG, and MG electrodes can be readily observed at various current densities (1.0, 2.0, and 3.0 mA cm⁻²) at a fixed capacity of 1.0 mAh cm⁻² (Fig. 3c–e). The MG electrodes showed a rapid decline in CE after 150, 130, and 100 cycles at current densities of 1.0, 2.0, and 3.0 mA cm⁻², respectively, whereas the WMG electrodes maintained stable CE profiles up to 200 cycles under the same conditions before gradually decreasing (Fig. 3c–e). In contrast, the HWMG electrodes exhibited significantly improved performance, maintaining stable operation for over 300, 450, and 450 cycles at 1.0, 2.0, and 3.0 mA cm⁻², respectively, highlighting their superior long-term stability (Fig. 3c–e). When comparing the average CE values over cycles for the HWMG electrodes with previously reported host materials at various current densities (0.5, 1.0, and 2.0 mA cm⁻²), the HWMG electrode showed comparable average CE and cycle stability with the best hosts reported to date (Fig. 3f and Table S7) [23,24,54–67].

Furthermore, symmetrical cell configurations (Li@HWMG||Li) were tested to measure the voltage hysteresis during the Li plating/stripping processes and the long-term stability of the samples. After the stabilization used for the asymmetric cell test, pre-plating with Li of the HWMG, WMG, and MG hosts was carried out by electrochemical deposition at a current density of 0.5 mA cm⁻² until a capacity of 15.0 mAh cm⁻² was reached. At a current density of 0.5 mA cm⁻² with a capacity of 1.0 mAh cm⁻², both the Li@HWMG and Li@WMG electrodes demonstrated stable early-stage Li plating/stripping with a very low overpotential of ca. 7 mV (Fig. 3g). However, when comparing their long-term stability, the Li@HWMG electrode exhibited excellent electrochemical stability for over 6000 h, whereas the Li@WMG electrode began to degrade after 4500 h. Conversely, the Li@MG electrode showed a higher overpotential (18 mV) for 800 h, eventually experiencing a short circuit after 1000 h (Fig. 3g). Under conditions of 2.0 mA cm⁻² and 4.0 mAh cm⁻², the Li@HWMG electrode maintained a low overpotential of about 8 mV for over 2000 h (Fig. 3h); in contrast, the Li@WMG electrode maintained an overpotential of about 15 mV for up to 1200 h but began to degrade thereafter. Meanwhile, the Li@MG electrode exhibited more than twice the overpotential of Li@HWMG and short-circuited at 900 h (Fig. 3h).

When tested under current densities of 2.0, 3.0, and 5.0 mA cm⁻² with a capacity of 1.0 mAh cm⁻², the Li@HWMG electrode consistently demonstrated stable performance with low overpotentials compared with the other electrodes (Fig. 3i–k). At a current density of 2.0 and 3.0 mA cm⁻², the Li@HWMG electrode showed low overpotentials of about 9 mV for 4000 h and 13 mV for 3500 h, respectively; in contrast, Li@WMG and Li@MG electrodes exhibited higher overpotentials of 18 and 20 mV at 2.0 mA cm⁻², and 19 and 27 mV at 3.0 mA cm⁻², respectively, for shorter durations (Fig. 3i, j). Furthermore, at 5.0 mA cm⁻², the Li@HWMG electrode demonstrated stable operation with an overpotential of 25 mV for 550 h, clearly demonstrating the potential to operate at high current density; in contrast, the Li@WMG and Li@MG electrodes were unable to sustain operation under these conditions (Fig. 3k). To efficiently assess temperature effects, rate performance was measured at 25 and 60 °C (Fig. S17). At 60 °C, the overpotential at a given current density was reduced by about twofold compared with that at 25 °C. When comparing the overpotentials of the Li@HWMG electrode over time with those of the best previously reported host materials, the Li@HWMG electrode exhibited a lower overpotential and superior long-term stability (Fig. 3l and Table S8) [26,29,39,40,54,65,68–74]. The electrochemical results of the asymmetric and symmetric cell tests clearly demonstrate

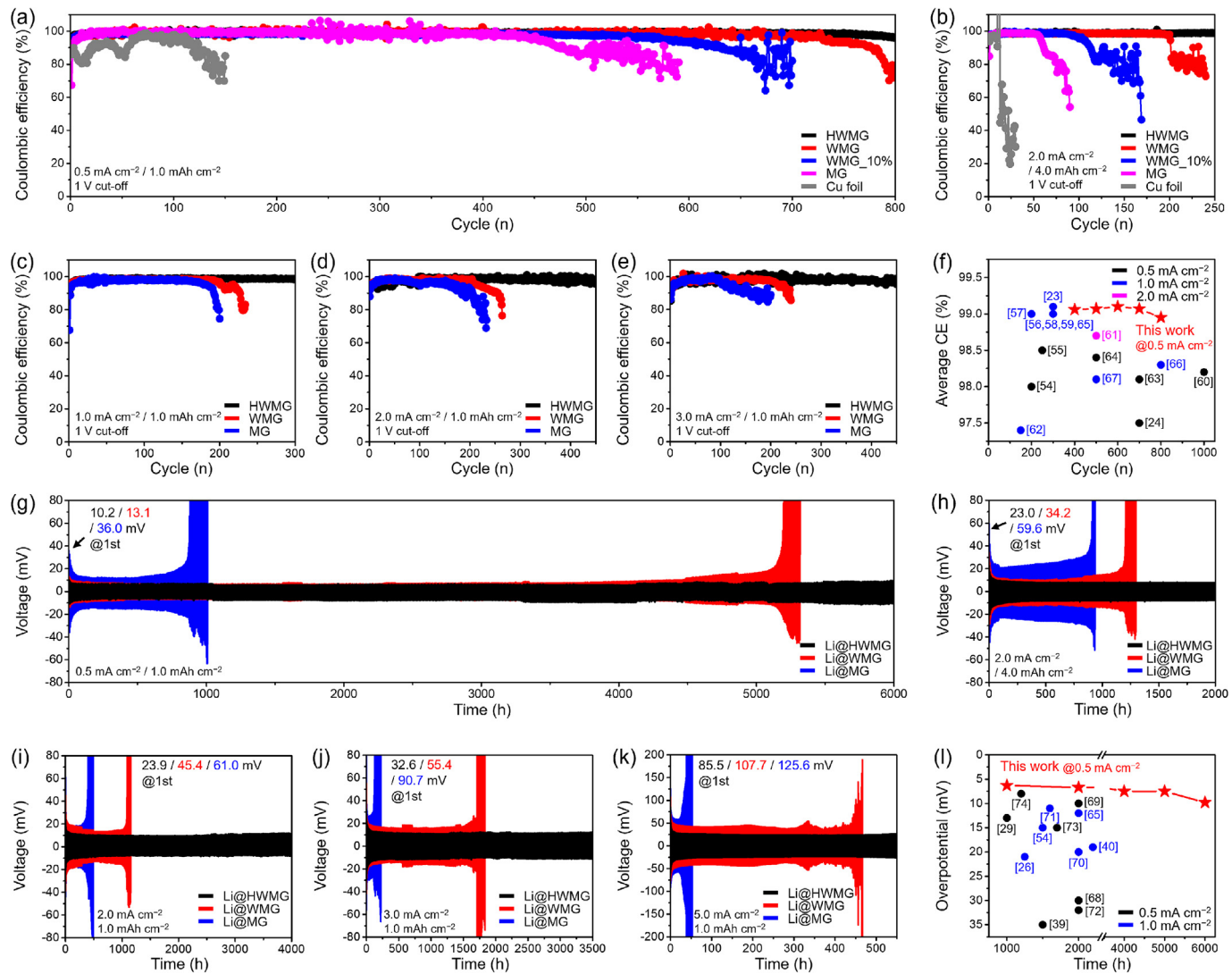


Fig. 3. Electrochemical performances of half-cells. CE performance of HWMG, WMG, WMG-10%, MG, and Cu foil at 0.5 mA cm^{-2} and 1.0 mAh cm^{-2} (a) and at 2.0 mA cm^{-2} and 4.0 mAh cm^{-2} (b). CE performance of HWMG, WMG, and MG electrodes at 1.0 mA cm^{-2} (c), 2.0 mA cm^{-2} (d), and 3.0 mA cm^{-2} (e) with 1.0 mAh cm^{-2} . CE performance comparison of HWMG electrode with host materials for LMAs (f). Overpotential of Li@HWMG, Li@WMG, and Li@MG electrodes at 0.5 mA cm^{-2} and 1.0 mAh cm^{-2} (g) and at 2.0 mA cm^{-2} and 4.0 mAh cm^{-2} (h). Overpotential of Li@HWMG, Li@WMG, and Li@MG electrodes at 2.0 mA cm^{-2} (i), 3.0 mA cm^{-2} (j), and 5.0 mA cm^{-2} (k) with 1.0 mAh cm^{-2} . Overpotential and long-term stability comparison of HWMG electrode with host materials for LMAs (l).

the advantageous features of the binder-free HWMG electrode, originating from its excellent adhesion, low tortuosity, flexibility, and high electrical conductivity, which play key roles in achieving facile Li-ion flux and efficient Li plating/stripping processes.

Furthermore, the electrochemical performance of the full-cell configurations of Li@HWMG, Li@WMG, and Li@MG with a LiFePO₄ (LFP) cathode (Li@HWMG||LFP, Li@WMG||LFP, and Li@MG||LFP) was evaluated with two initial stabilization cycles at 0.1 C ($1 \text{ C} = 170 \text{ mA g}_{\text{LFP}}^{-1}$). At a high cathode loading level (31.6 mg cm^{-2} , theoretical capacity of 4.52 mAh cm^{-2}), the galvanostatic charge/discharge processes of all full cells were conducted at various C rates. The Li@MG||LFP full cell exhibited poor performance across all rates due to high tortuosity and binder effects. In contrast, Li@HWMG||LFP and Li@WMG||LFP showed similar performance at lower rates, but Li@HWMG||LFP outperformed Li@WMG||LFP at higher rates due to lower tortuosity (Fig. 4a and Fig. S18). In addition, when long-term stability for all full cells was tested at 1 C , Li@HWMG||LFP demonstrated superior performance, maintaining an average CE of 99.6 % over 700 cycles with capacity retentions of 86.7 % (100 cycles), 75.4 % (300 cycles), 69.1 % (500 cycles),

and 66.1 % (700 cycles) compared to the 3rd cycle (3.36 mAh cm⁻²). In comparison, Li@WMG||LFP exhibited stable performance up to 50 cycles but showed a rapid decline in capacity retention thereafter. Meanwhile, Li@MG||LFP demonstrated significantly lower performance, with an unstable capacity profile and rapid fading from the beginning (Fig. 4b). In addition, when tested at 0.5 C , Li@HWMG||LFP showed superior electrochemical performance to the others (please see Fig. S19 in detail).

Moreover, when a much higher cathode loading level (ca. 36.8 mg cm^{-2} , theoretical capacity of 5.01 mAh cm^{-2}) was applied at 0.3C , Li@HWMG||LFP again demonstrated remarkable performance, achieving an initial areal capacity of 4.06 mAh cm^{-2} and retaining 91.5 % (3.57 mAh cm^{-2}) after 200 cycles and 85.6 % (3.34 mAh cm^{-2}) after 350 cycles compared to the 3rd cycle (3.90 mAh cm^{-2}). Meanwhile, the Li@WMG||LFP and Li@MG||LFP electrodes exhibited similar initial capacities of 4.18 and 2.88 mAh cm^{-2} , respectively. However, while Li@WMG||LFP maintained stable capacity retention up to 200 cycles (81.0 %, 3.20 mAh cm^{-2}) before experiencing rapid degradation, Li@MG||LFP showed a significant capacity decline from the beginning, high-

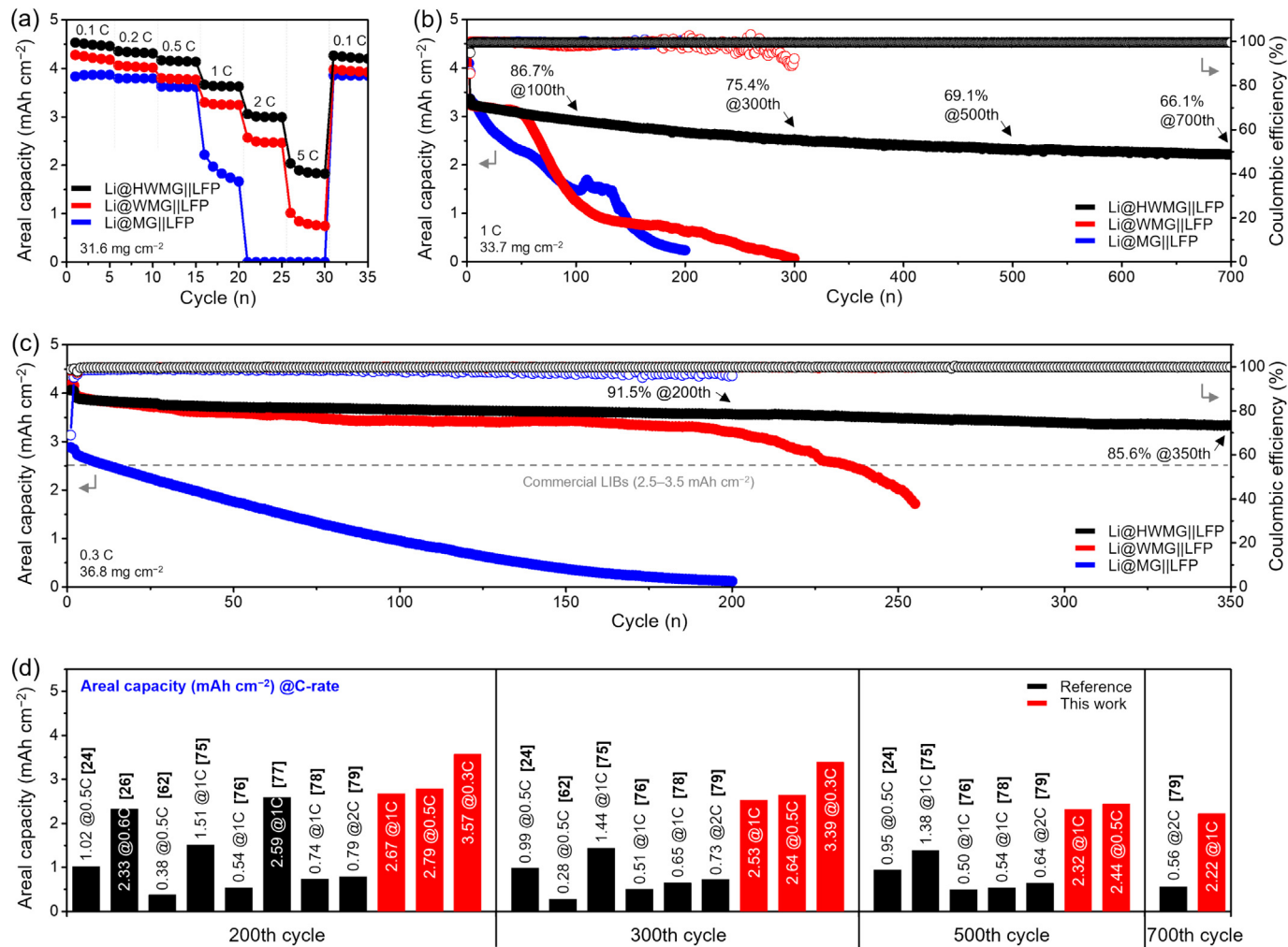


Fig. 4. Electrochemical performances of full-cells. Rate performance of Li@HWMG||LFP, Li@WMG||LFP, and Li@MG||LFP full cells (a). Cycle performance of Li@HWMG||LFP, Li@WMG||LFP, and Li@MG||LFP full cells at 1 C (b) and 0.3 C (c). Areal capacity comparison at the 200th, 300th, 500th, and 700th cycle of Li@HWMG||LFP full cells with host materials for LMAs using ether electrolyte (d).

lighting the superior long-term stability and performance of Li@HWMG||LFP (Fig. 4c). When comparing areal capacities obtained in this study with previously reported best values using ether-based electrolytes (Fig. 4d), our results exhibited superior performances after the 200th, 300th, 500th, and 700th cycles (Table S9) [24, 26, 62, 75–79]. This sustained long-term stability underscores the industrial potential of the HWMG host for LMAs, demonstrating its ability to reliably address the requirements of practical applications that demand both high capacity and long-term cycle life.

2.4. Influences of tortuosity and binder on electrochemical performance

The nucleation overpotential was measured to assess the lithiophilicity of the scaffolds and their ability to induce uniform Li plating. At a current density of 0.5 mA cm⁻² for Li plating, the relatively lithiophobic Cu foil showed a high overpotential of 44.8 mV, whereas the lithiophilic rGO-based hosts (HWMG, WMG, WMG_10%, and MG) displayed similar overpotentials of approximately 28 mV, validating their suitability as scaffolds (Fig. 5a and Table S10). Next, we focused on the point (time) at which nucleation begins. The time required for nucleation varies depending on the diffusion rate of Li-ions and the electron transfer rate of

the electrode, which are influenced by the tortuosity and electrical conductivity of the electrode, respectively [26, 38–40, 66]. The time of voltage dip pointing to the nucleation is designated as the “onset time” in this study, which denotes the point at which Li-ions are reduced on the scaffold surface. It has been consistently observed that host-less substrates, such as the Cu current collector, exhibited near-zero onset times, while the onset times of various scaffolds increased with reduced mobility of Li-ions [66, 67, 71, 80–82]. Thus, onset time is substantially associated with the tortuosity and electrical conductivity of the electrode.

The onset times of HWMG, WMG, WMG_10%, and MG electrodes at various current densities (0.5, 1.0, and 2.0 mA cm⁻²) are displayed and listed in Fig. 5(b), Fig. S20, and Table S10. At a low current density (e.g., 0.5 mA cm⁻²), the onset times of the HWMG, WMG, WMG_10%, and MG electrodes were significantly different, being 0.47, 0.85, 1.42, and 2.33 h, respectively. These results indicated that the binder-free HWMG electrode with the lowest tortuosity and high electrical conductivity exhibited the fastest onset time. The binder effect was also observed when comparing WMG and WMG_10% electrodes, clearly confirming the inferior effect on tortuosity and electrical conductivity. Lastly, the MG electrode exhibited the slowest onset time owing to its high tortuosity and the use of a binder. Conversely, the differences in the onset times of the samples became more similar at higher current densities,

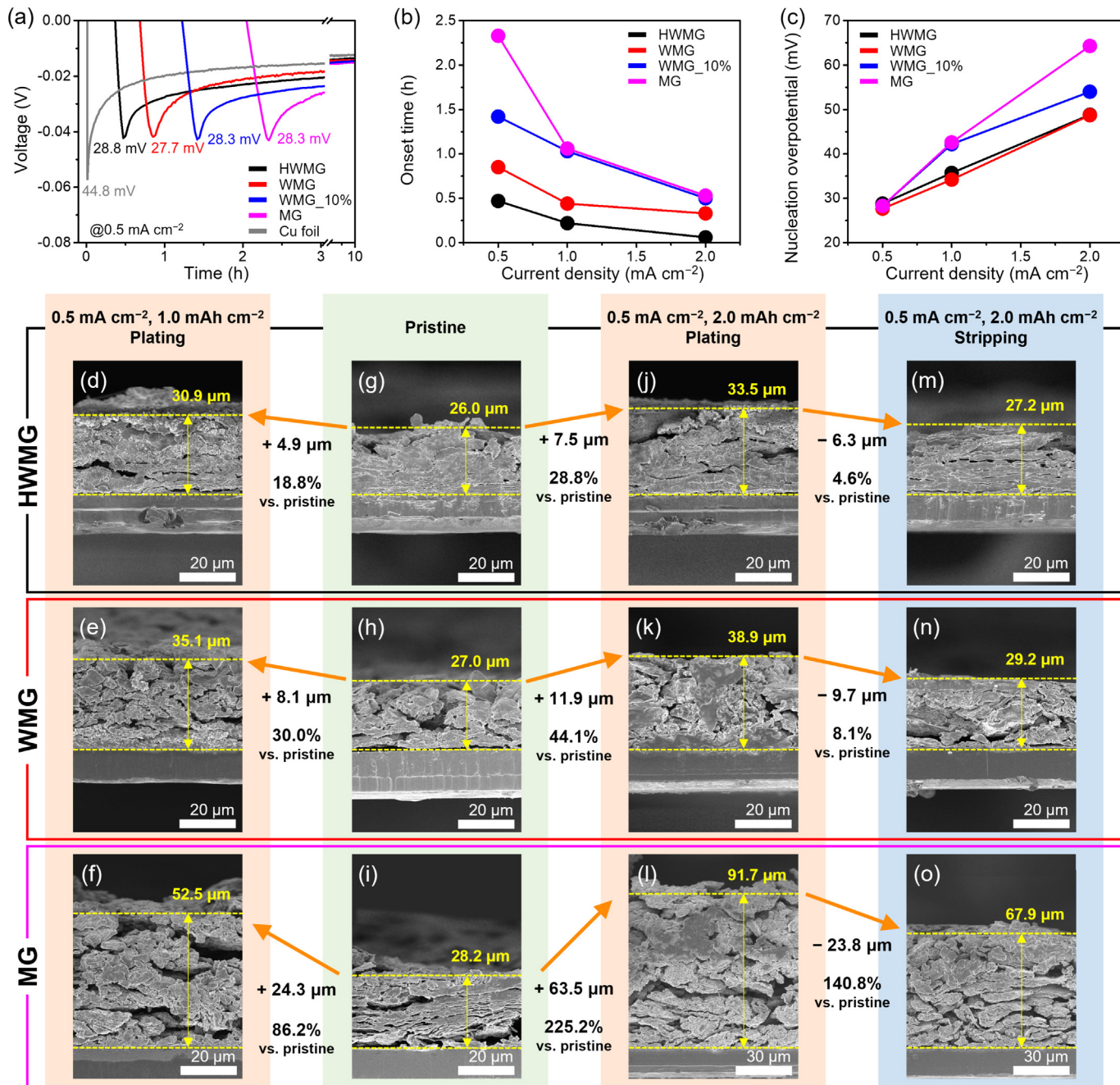


Fig. 5. Tortuosity and binder effect on initial Li plating and stripping. Nucleation overpotential differences for HWMG, WMG, WMG_{10%}, MG, and Cu foil at a current density of 0.5 mA cm^{-2} (a). Nucleation onset time (b) and overpotential comparison (c) for HWMG, WMG, WMG_{10%}, and MG at different current densities. Cross-sectional SEM images of HWMG (d), WMG (e), and MG electrodes (f) after the first Li plating at 0.5 mA cm^{-2} and 1.0 mAh cm^{-2} . Cross-sectional SEM images of HWMG (g), WMG (h), and MG electrodes (i) in the initial state. Cross-sectional SEM images of HWMG (j), WMG (k), and MG electrodes (l) after the first Li plating at 0.5 mA cm^{-2} and 2.0 mAh cm^{-2} . Cross-sectional SEM images of HWMG (m), WMG (n), and MG electrodes (o) after the first Li stripping at 0.5 mA cm^{-2} and 2.0 mAh cm^{-2} .

presumably because of the reduction in the tortuosity effect at higher current densities (Fig. 5b, Fig. S20, and Table S10). Additionally, as the current density increased, the previously similar nucleation overpotential exhibited a tendency to increase. Notably, the magnitude of this increase was more pronounced in electrodes containing a binder, suggesting that the binder negatively affects the nucleation barrier (Fig. 5c, Fig. S20, and Table S10). Therefore, these results emphasize the impact of the tortuosity and binder of the electrode on the nucleation barrier and onset time during Li plating/stripping processes [83].

To further explore the volume changes of the electrodes during consecutive plating/stripping processes, a cross-sectional SEM

investigation was conducted. After Li plating at a current density of 0.5 mA cm^{-2} and a capacity of 1.0 mAh cm^{-2} , the thicknesses of HWMG, WMG, WMG_{10%}, and MG increased to 30.9, 35.1, 39.8, and $52.5 \mu\text{m}$, respectively, from the pristine samples (Fig. 5d–i and Fig. S21a, b). The smallest thickness change was observed for the HWMG electrode, followed by the WMG and WMG_{10%} electrode, whereas the MG electrode showed the largest thickness variation. Furthermore, the differences in thickness change became more pronounced, following the order HWMG < WMG < WMG_{10%} < MG at a capacity of 2.0 mAh cm^{-2} (Fig. 5j–l and Fig. S21c). These trends can be attributed to the tortuosity effect and electrical conductivity of the electrodes; the

porous and binder-free HWMG exhibited the lowest volume change upon Li plating. Furthermore, after Li stripping, HWMG, WMG, and WMG_10% were nearly restored to their original thicknesses (27.2, 29.2, and 31.9 μm , respectively, compared to the pristine samples of 26.0, 27.0, and 27.3 μm , respectively) owing to the inherent resilience properties of their wrinkled and multilayered features (Fig. 5g, h, m, n, Figs. S15 and S21). Conversely, a significant difference was observed for the MG electrode (67.9 μm) compared with the pristine (28.2 μm) after Li stripping due to its less flexible mechanical feature (Fig. 5i, o, and Fig. S15).

In addition, EIS measurements of the HWMG, WMG, and MG electrodes were conducted after 100 cycles (after the stripping state of the asymmetric cell test at a current density of 0.5 mA cm^{-2} and a capacity of 1.0 mAh cm^{-2}) (Fig. 6a, b, and Fig. S22). After 100 cycles, the charge transfer resistance (R_{ct}) and the resistance associated with the solid electrolyte interphase (R_{SEI}) obtained by fitting to an equivalent circuit showed distinct differences among the electrodes. The MG electrode showed R_{SEI} of 15.94 Ω and R_{ct} of 36.70 Ω , while the WMG electrode exhibited R_{SEI} of 11.20 Ω and R_{ct} of 9.01 Ω (Fig. 6a, b, and Table S11). In contrast, the HWMG electrode maintained the lowest R_{SEI} of 9.95 Ω and R_{ct} of 10.55 Ω , highlighting the impact of its structural properties (Fig. 6a, b, and Table S11). The HWMG and WMG electrodes exhibited smaller values of R_{SEI} and R_{ct} than those of the MG electrode after 100 cycles. Low tortuosity and mechanical flexibility maintain a stable electrode structure during cycling and promote stable solid electrolyte interphase (SEI) layer formation. In addition, high electrical conductivity together with low tortuosity limits uneven Li plating in the upper part of the electrode, suppressing dendrite growth. This suppression reduces the accumulation of dead Li and thereby lowers R_{ct} [26,29,59].

To understand the EIS results, a cross-sectional SEM investigation of the electrodes was conducted after 10 and 100 cycles (Fig. 6c, d and Fig. S23a, b). The thicknesses of the HWMG electrode after 10 and 100 cycles were 26.9 μm (3 % increase) and 28.5 μm (10 % increase), respectively, compared to the pristine (26.0 μm) (Fig. 5g). The increase trend was slightly higher for the WMG electrode that the thicknesses after 10 and 100 cycles were 28.8 μm (7 % increase) and 34.0 μm (26 % increase), respectively, compared to the pristine (27.0 μm) (Fig. 5h). In contrast, the thicknesses of the MG electrode after 10 and 100 cycles were 39.3 μm (39 % increase) and 59.2 μm (110 % increase), respectively, compared to the pristine (28.2 μm) (Fig. 5i). It is clear that the upper part of the MG electrode was mainly used as a host for Li plating/stripping because of its high tortuosity combined with its inability to buffer volume expansion, resulting in more dendrite growth and the continuous formation of an SEI layer over repeated cycles (Fig. 6d), which is consistent with the EIS analysis.

In-plane SEM investigations of the HWMG, WMG, and MG electrodes were performed after 10 and 100 cycles (Fig. 6e–j and Fig. S23c–e). After 10 cycles, the HWMG electrode showed a relatively smooth surface with uneven features instead of sharp dendrites, highlighting its ability to suppress dendritic growth effectively (Fig. 6e). In comparison, the WMG electrode exhibited small and scattered dendrites, while the MG electrode showed more pronounced dendritic formations on its surface (Fig. 6h and Fig. S23c). These observations reflect the efficient Li-ion flux of the HWMG electrode. After 100 cycles, the differences in the dendritic growth became more pronounced. The surface of the MG electrode was heavily covered with vertically grown Li dendrites (Fig. 6i, j), whereas the HWMG electrode maintained its smooth and uneven surface (Fig. 6f, g), and the WMG electrode showed

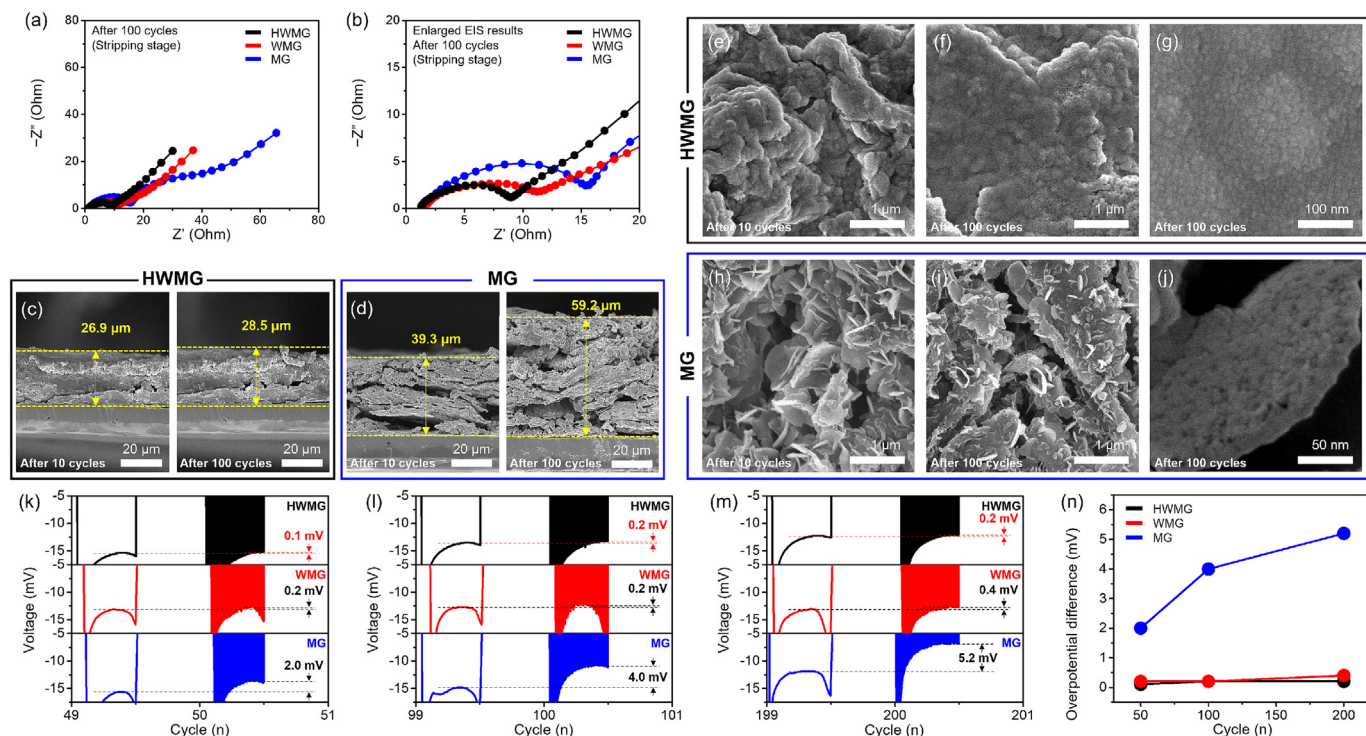


Fig. 6. Tortuosity and binder effects on various stages of cycling. EIS results of the asymmetric cell test for HWMG, WMG, and MG electrodes at 0.5 mA cm^{-2} and 1.0 mAh cm^{-2} after 100 cycles at the Li stripping stage, with the overall plots (a) and a magnified section (b). Cross-sectional SEM images after Li stripping at 0.5 mA cm^{-2} and 1.0 mAh cm^{-2} for the asymmetric cell test after 10 cycles and 100 cycles for HWMG (c) and MG electrodes (d). Top view SEM images of after Li stripping at 0.5 mA cm^{-2} and 1.0 mAh cm^{-2} for the asymmetric cell test after 10 cycles for HWMG (e) and MG electrodes (h), and after 100 cycles for HWMG (f), enlarged HWMG (g), MG (i), and enlarged MG electrodes (j). GITT voltage profiles of HWMG, WMG, and MG electrodes at 0.5 mA cm^{-2} and 0.5 mAh cm^{-2} for the 50th (k), 100th (l), and 200th (m) cycles, along with a comparison of plateau overpotential differences across various cycles (n).

only a slight increase in dendrite size compared to that after 10 cycles (Fig. S23d, e). In particular, porous features of the MG surface were clearly observed after 100 cycles, strongly suggesting the continuous formation of Li dendrites and SEI layers over the cycles [28,56,62]. Therefore, the low tortuosity, high electrical conductivity, and resilience characteristics of the HWMG electrode play a crucial role in suppressing dendritic growth, preventing the disruption of the SEI layer, avoiding exposure of new surfaces, and resulting in the uniform distribution of Li-ion flux across the electrode. To examine whether the HWMG scaffold changes the SEI composition, XPS was performed on the HWMG electrode and Cu foil after five cycles in an asymmetric cell at a current density of 0.5 mA cm^{-2} and a capacity of 1.0 mAh cm^{-2} (Fig. S24). The O 1s and F 1s spectra showed similar peak positions on both substrates, indicating similar SEI constituents.

Furthermore, galvanostatic intermittent titration technique (GITT) was conducted to analyze the efficient electrochemical movement of Li-ions within the HWMG, WMG, and MG electrodes. Because the formation of a quasi-steady-state concentration gradient within the electrolyte inside the electrode is a time-dependent process, GITT minimizes the effect of changes in the Li-ion concentration gradient within the electrode on cell polarization. After a long relaxation period in GITT, Li metal can be plated under equilibrium conditions [84–86]. GITT tests, consisting of 15-second short current pulses followed by 180-second rest periods at a current density of 0.5 mA cm^{-2} and a capacity of 0.5 mAh cm^{-2} , were conducted at the 50th, 100th, and 200th cycles (Fig. 6k–n and Fig. S25). By comparing these galvanostatic cycles (asymmetric cell test results) with the GITT cycles, the differences in the overpotential in the plateau region (plateau overpotential) between the electrodes were analyzed. At the 50th GITT cycle, the overpotential difference between the plateau regions of the 50th and 49th cycles of HWMG and WMG electrodes was 0.1 and 0.2 mV, while the MG electrode showed a much larger difference of 2.0 mV (Fig. 6k and Fig. S25a). Upon reaching the 100th cycle, the HWMG and WMG electrodes exhibited a slight increase to 0.2 mV, while the MG electrode showed an increased difference of 4.0 mV (Fig. 6l and Fig. S25b). At the 200th cycle, the HWMG electrode maintained a steady overpotential difference of 0.2 mV, the WMG electrode increased to 0.4 mV, and the MG electrode further increased to 5.2 mV, reflecting the growing disparity among the electrodes (Fig. 6m and Fig. S25c). From the 50th to the 200th cycle, the HWMG electrode exhibited the lowest potential differences, with the WMG electrode showing similar differences. In contrast, the MG electrode showed a progressively larger difference (Fig. 6n). These results indicate that the overpotential difference is governed primarily by tortuosity. With extended cycling, the HWMG electrode maintained a nearly unchanged plateau overpotential, consistent with cycle stability enabled by its mechanical flexibility and higher electrical conductivity. In contrast, the MG electrode showed a growing plateau overpotential as cycling proceeded, which was attributed to its higher tortuosity and lower conductivity. The HWMGO_8h and HWMG electrodes were prepared via a solution-based process involving a mild oxidative treatment and drying. Owing to its simple and scalable synthesis route, the production cost is considered comparable to that of conventional functional graphene-based electrodes (Table S12).

3. Conclusions

In summary, the utilization of HWMG as a binder-free host for LMAs significantly enhanced their electrochemical performance and long-term stability. The unique properties of HWMG, including outstanding mechanical flexibility, adhesion, high porosity, wrinkled morphology, and low tortuosity, allow for efficient accommo-

dation of volume changes, enabling uniform Li-ion flux across the electrode, thereby suppressing dendrite growth and buffering volume expansion. The binder-free HWMG hosts demonstrated remarkable electrochemical performance, with an average CE of 98.9 % over 800 cycles in the asymmetric cell test and a low voltage hysteresis of approximately 7 mV over 6000 h in the symmetric cell test. Additionally, full-cell tests with LFP cathodes confirmed the practical viability of the HWMG with an areal capacity of 3.34 mAh cm^{-2} (85.6 % capacity retention) after 350 cycles, even at a high cathode mass loading. These results highlight the important role of electrode morphology, mechanical flexibility, and binder effects in improving the electrochemical performance and long-term stability of LMAs. The HWMG scaffold offers a promising solution for developing high-energy-density LIBs, addressing the key challenges associated with LMAs and advancing their commercialization in advanced energy storage systems.

Experimental section

Experimental details can be found in the [Supporting Information](#).

CRediT authorship contribution statement

Sangyeop Kim: Writing – review & editing, Writing – original draft, Validation, Methodology, Investigation, Data curation, Conceptualization. **Incheol Heo:** Validation, Investigation. **Jun Hyuk Kang:** Writing – review & editing, Formal analysis. **Min Seok Kang:** Validation. **Junsung Lee:** Investigation. **Hee Soo Kim:** Funding acquisition. **Dong-Ha Lim:** Funding acquisition. **Sung Beom Cho:** Writing – review & editing, Funding acquisition. **Won Cheol Yoo:** Writing – review & editing, Writing – original draft, Supervision, Project administration, Methodology, Funding acquisition, Conceptualization.

Declaration of competing interest

The authors declare that they have no known competing financial interests or personal relationships that could have appeared to influence the work reported in this paper.

Acknowledgments

This work was supported by the National Research Foundation of Korea (NRF) grants funded by the Korean government (MSIT) (RS-2024-00409952, RS-2024-00347936, and RS-2024-00407282). This work was supported by the GRRC Program of Gyeonggi Province (GRRCHanyang2020-B01). This work was also supported by the Commercialization Promotion Agency for R&D Outcomes (COMPA) grant funded by the Korean Government (MSIT) (RS-2023-00304763).

Appendix A. Supplementary material

Supplementary data to this article can be found online at <https://doi.org/10.1016/j.jecem.2025.09.025>.

References

- [1] D. Lin, Y. Liu, Y. Cui, Nat. Nanotechnol. 12 (2017) 194–206. <https://doi.org/10.1038/nnano.2017.16>.
- [2] W. Xu, J. Wang, F. Ding, X. Chen, E. Nasybulin, Y. Zhang, J.-G. Zhang, Energy Environ. Sci. 7 (2014) 513–537. <https://doi.org/10.1039/C3EE40795K>.
- [3] J. Liu, Z. Bao, Y. Cui, E.J. Dufek, J.B. Goodenough, P. Khalifah, Q. Li, B.Y. Liaw, P. Liu, A. Manthiram, Y.S. Meng, V.R. Subramanian, M.F. Toney, V.V. Viswanathan, M.S. Whittingham, J. Xiao, W. Xu, J. Yang, X.-Q. Yang, J.-G. Zhang, Nat. Energy 4 (2019) 180–186. <https://doi.org/10.1038/s41560-019-0338-x>.

- [4] B. Liu, J.-G. Zhang, W. Xu, Joule 2 (2018) 833–845. <https://doi.org/10.1016/j.joule.2018.03.008>.
- [5] Y. Guo, H. Li, T. Zhai, Adv. Mater. 29 (2017) 1700007. <https://doi.org/10.1002/adma.201700007>.
- [6] J.M. Tarascon, M. Armand, Nature 414 (2001) 359–367. <https://doi.org/10.1038/35104644>.
- [7] X.-B. Cheng, R. Zhang, C.-Z. Zhao, Q. Zhang, Chem. Rev. 117 (2017) 10403–10473. <https://doi.org/10.1021/acs.chemrev.7b00115>.
- [8] Y. Xia, P. Zhou, X. Kong, J. Tian, W. Zhang, S. Yan, W.-H. Hou, H.-Y. Zhou, H. Dong, X. Chen, P. Wang, Z. Xu, L. Wan, B. Wang, K. Liu, Nat. Energy 8 (2023) 934–945. <https://doi.org/10.1038/s41560-023-01282-z>.
- [9] W. Li, H. Yao, K. Yan, G. Zheng, Z. Liang, Y.-M. Chiang, Y. Cui, Nat. Commun. 6 (2015) 7436. <https://doi.org/10.1038/ncomms8436>.
- [10] M. Cheng, X. Zhou, Y. Liang, Y. Zheng, J. Energy Chem. 108 (2025) 759–768. <https://doi.org/10.1016/j.jechem.2025.04.069>.
- [11] J. Bae, Y. Qian, Y. Li, X. Zhou, J.B. Goodenough, G. Yu, Energy Environ. Sci. 12 (2019) 3319–3327. <https://doi.org/10.1039/C9EE02558H>.
- [12] Z. Lin, Y. Ma, W. Wang, Y. He, M. Wang, J. Tang, C. Fan, K. Sun, J. Energy Chem. 76 (2023) 631–638. <https://doi.org/10.1016/j.jechem.2022.09.030>.
- [13] C. Yan, X.-B. Cheng, Y. Tian, X. Chen, X.-Q. Zhang, W.-J. Li, J.-Q. Huang, Q. Zhang, Adv. Mater. 30 (2018) 1707629. <https://doi.org/10.1002/adma.201707629>.
- [14] A. Hu, W. Chen, X. Du, Y. Hu, T. Lei, H. Wang, L. Xue, Y. Li, H. Sun, Y. Yan, J. Long, C. Shu, J. Zhu, B. Li, X. Wang, J. Xiong, Energy Environ. Sci. 14 (2021) 4115–4124. <https://doi.org/10.1039/D1EE00508A>.
- [15] W. Tang, S. Tang, X. Guan, X. Zhang, Q. Xiang, J. Luo, Adv. Funct. Mater. 29 (2019) 1900648. <https://doi.org/10.1002/adfm.201900648>.
- [16] P. Chen, P. Guo, W. Guo, B. Ding, H. Dou, X. Zhang, J. Energy Chem. 110 (2025) 363–371. <https://doi.org/10.1016/j.jechem.2025.06.070>.
- [17] X.-B. Cheng, M.-Q. Zhao, C. Chen, A. Pentecost, K. Maleski, T. Mathis, X.-Q. Zhang, Q. Zhang, J. Jiang, Y. Gogotsi, Nat. Commun. 8 (2017) 336. <https://doi.org/10.1038/s41467-017-00519-2>.
- [18] Y. Liu, Y.-K. Tzeng, D. Lin, A. Pei, H. Lu, N.A. Melosh, Z.-X. Shen, S. Chu, Y. Cui, Joule 2 (2018) 1595–1609. <https://doi.org/10.1016/j.joule.2018.05.007>.
- [19] M.D. Tikekar, S. Choudhury, Z. Tu, L. Archer, Nat. Energy 1 (2016) 16114. <https://doi.org/10.1038/nenergy.2016.114>.
- [20] W. Guo, S. Liu, X. Guan, X. Zhang, X. Liu, J. Luo, Adv. Energy Mater. 9 (2019) 1900193. <https://doi.org/10.1002/aenm.201900193>.
- [21] X. He, K. Zhang, Z. Zhu, Z. Tong, X. Liang, Chem. Soc. Rev. 53 (2024) 9–24. <https://doi.org/10.1039/D3CS00495C>.
- [22] T. Lyu, F. Luo, D. Wang, L. Bu, L. Tao, Z. Zheng, Adv. Energy Mater. 12 (2022) 2201493. <https://doi.org/10.1002/aenm.202201493>.
- [23] H. Chen, A. Pei, J. Wan, D. Lin, R. Vilá, H. Wang, D. Mackanic, H.-G. Steinrück, W. Huang, Y. Li, A. Yang, J. Xie, Y. Wu, H. Wang, Y. Cui, Joule 4 (2020) 938–952. <https://doi.org/10.1016/j.joule.2020.03.008>.
- [24] S. Liu, A. Wang, Q. Li, J. Wu, K. Chiou, J. Huang, J. Luo, Joule 2 (2018) 184–193. <https://doi.org/10.1016/j.joule.2017.11.004>.
- [25] D. Lin, Y. Liu, Z. Liang, H.-W. Lee, J. Sun, H. Wang, K. Yan, J. Xie, Y. Cui, Nat. Nanotechnol. 11 (2016) 626–632. <https://doi.org/10.1038/nnano.2016.32>.
- [26] Q. Wu, M. Qin, H. Yan, W. Zhong, W. Zhang, M. Liu, S. Cheng, J. Xie, ACS Appl. Mater. Interfaces 14 (2022) 42030–42037. <https://doi.org/10.1021/acsmami.2c10920>.
- [27] S.-S. Chi, Y. Liu, W.-L. Song, L.-Z. Fan, Q. Zhang, Adv. Funct. Mater. 27 (2017) 1700348. <https://doi.org/10.1002/adfm.201700348>.
- [28] A.M. Hafez, Y. Jiao, J. Shi, Y. Ma, D. Cao, Y. Liu, H. Zhu, Adv. Mater. 30 (2018) 1802156. <https://doi.org/10.1002/adma.201802156>.
- [29] Q. Song, H. Yan, K. Liu, K. Xie, W. Li, W. Gai, G. Chen, H. Li, C. Shen, Q. Fu, S. Zhang, L. Zhang, B. Wei, Adv. Energy Mater. 8 (2018) 1800564. <https://doi.org/10.1002/aenm.201800564>.
- [30] G. Zheng, S.W. Lee, Z. Liang, H.-W. Lee, K. Yan, H. Yao, H. Wang, W. Li, S. Chu, Y. Cui, Nat. Nanotechnol. 9 (2014) 618–623. <https://doi.org/10.1038/nnano.2014.152>.
- [31] X. Chen, X.-R. Chen, T.-Z. Hou, B.-Q. Li, X.-B. Cheng, R. Zhang, Q. Zhang, Sci. Adv. 5 (2019) eaau7728. <https://doi.org/10.1126/sciadv.aau7728>.
- [32] R. Zhang, X.-R. Chen, X. Chen, X.-B. Cheng, X.-Q. Zhang, C. Yan, Q. Zhang, Angew. Chem. Int. Ed. 56 (2017) 7764–7768. <https://doi.org/10.1002/anie.201702099>.
- [33] T. Yang, L. Li, F. Wu, R. Chen, Adv. Funct. Mater. 30 (2020) 2002013. <https://doi.org/10.1002/adfm.202002013>.
- [34] T. Wang, P. Zhai, D. Legut, L. Wang, X. Liu, B. Li, C. Dong, Y. Fan, Y. Gong, Q. Zhang, Adv. Energy Mater. 9 (2019) 1804000. <https://doi.org/10.1002/aenm.201804000>.
- [35] W. Huang, Y. Yu, Z. Hou, Z. Liang, Y. Zheng, Z. Quan, Y.-C. Lu, Energy Storage Mater. 33 (2020) 329–335. <https://doi.org/10.1016/j.ensm.2020.08.032>.
- [36] J. Zhu, D. Cai, J. Li, X. Wang, X. Xia, C. Gu, J. Tu, Energy Storage Mater. 49 (2022) 546–554. <https://doi.org/10.1016/j.ensm.2022.05.001>.
- [37] H. Chen, Y. Yang, D.T. Boyle, Y.K. Jeong, R. Xu, L.S. de Vasconcelos, Z. Huang, H. Wang, H. Wang, W. Huang, H. Li, J. Wang, H. Gu, R. Matsumoto, K. Motohashi, Y. Nakayama, K. Zhao, Y. Cui, Nat. Energy 6 (2021) 790–798. <https://doi.org/10.1038/s41560-021-00833-6>.
- [38] Y. Shi, B. Li, Y. Zhang, Y. Cui, Z. Cao, Z. Du, J. Gu, K. Shen, S. Yang, Adv. Energy Mater. 11 (2021) 2003663. <https://doi.org/10.1002/aenm.202003663>.
- [39] Z. Zhu, B. Liu, Y. Qian, Y. Fang, X. Lei, X. Liu, J. Zhou, Y. Qian, G. Wang, Adv. Energy Mater. 13 (2023) 2203687. <https://doi.org/10.1002/aenm.202203687>.
- [40] X. Zhu, H. Cheng, S. Lyu, J. Huang, J. Gu, Y. Guo, Y. Peng, J. Liu, C. Wang, J. Duan, S. Yang, Adv. Energy Mater. 13 (2023) 2300129. <https://doi.org/10.1002/aenm.202300129>.
- [41] M.S. Kang, I. Heo, S. Kim, J. Yang, J. Kim, S.-J. Min, J. Chae, W.C. Yoo, Energy Storage Mater. 50 (2022) 234–242. <https://doi.org/10.1016/j.ensm.2022.05.025>.
- [42] H. Sun, L. Mei, J. Liang, Z. Zhao, C. Lee, H. Fei, M. Ding, J. Lau, M. Li, C. Wang, X. Xu, G. Hao, B. Papandrea, I. Shakir, B. Dunn, Y. Huang, X. Duan, Science 356 (2017) 599–604. <https://doi.org/10.1126/science.aam5852>.
- [43] Y. Xu, C.-Y. Chen, Z. Zhao, Z. Lin, C. Lee, X. Xu, C. Wang, Y. Huang, M.I. Shakir, X. Duan, Nano Lett. 15 (2015) 4605–4610. <https://doi.org/10.1021/acs.nanolett.5b01212>.
- [44] S. Park, K.-S. Lee, G. Bozoklu, W. Cai, S.T. Nguyen, R.S. Ruoff, ACS Nano 2 (2008) 572–578. <https://doi.org/10.1021/nm700349a>.
- [45] S.K. Perumal, S. Lee, H. Yu, J. Heo, M.J. Kang, Y. Kim, M. Park, H. Lee, H.S. Kim, ACS Appl. Mater. Interfaces 16 (2024) 7353–7363. <https://doi.org/10.1021/acsmami.3c18720>.
- [46] Y.J. Mai, M.P. Zhou, H.J. Ling, F.X. Chen, W.Q. Lian, X.H. Jie, Appl. Surf. Sci. 433 (2018) 232–239. <https://doi.org/10.1016/j.apsusc.2017.10.014>.
- [47] H. Wang, Q. Hao, X. Yang, L. Lu, X. Wang, Electrochim. Commun. 11 (2009) 1158–1161. <https://doi.org/10.1016/j.elecom.2009.03.036>.
- [48] D.R. Dreyer, S. Park, C.W. Bielawski, R.S. Ruoff, Chem. Soc. Rev. 39 (2010) 228–240. <https://doi.org/10.1039/B917103G>.
- [49] A.M. Dimiev, J.M. Tour, ACS Nano 8 (2014) 3060–3068. <https://doi.org/10.1021/nm500606a>.
- [50] Y. Liu, X. Gong, C. Podder, F. Wang, Z. Li, J. Liu, J. Fu, X. Ma, P. Vanaphuti, R. Wang, A. Hitt, Y. Savsatli, Z. Yang, M. Ge, W.-K. Lee, B. Yonemoto, M. Tang, H. Pan, Y. Wang, Joule 7 (2023) 952–970. <https://doi.org/10.1016/j.joule.2023.04.006>.
- [51] F. Pouraghajian, H. Knight, M. Wray, B. Mazzeo, R. Subbaraman, J. Christensen, D. Wheeler, J. Electrochem. Soc. 165 (2018) A2644. <https://doi.org/10.1149/2.0611811jies>.
- [52] J. Landesfeind, J. Hattendorff, A. Ehrl, W.A. Wall, H.A. Gasteiger, J. Electrochem. Soc. 163 (2016) A1373. <https://doi.org/10.1149/2.1141607jes>.
- [53] H. Chen, G. Zhou, D. Boyle, J. Wan, H. Wang, D. Lin, D. Mackanic, Z. Zhang, S.C. Kim, H.R. Lee, H. Wang, W. Huang, Y. Ye, Y. Cui, Matter 2 (2020) 1605–1620. <https://doi.org/10.1016/j.matt.2020.04.011>.
- [54] G. Huang, J. Han, F. Zhang, Z. Wang, H. Kashani, K. Watanabe, M. Chen, Adv. Mater. 31 (2019) 1805334. <https://doi.org/10.1002/adma.201805334>.
- [55] P. Zhai, T. Wang, W. Yang, S. Cui, P. Zhang, A. Nie, Q. Zhang, Y. Gong, Adv. Energy Mater. 9 (2019) 1804019. <https://doi.org/10.1002/aenm.201804019>.
- [56] Y. Ma, B. Yao, M. Zhang, H. Bai, G. Shi, J. Mater. Chem. A 6 (2018) 15603–15609. <https://doi.org/10.1039/C8TA04911D>.
- [57] L. Dong, L. Nie, W. Liu, Adv. Mater. 32 (2020) 1908494. <https://doi.org/10.1002/adma.201908494>.
- [58] N. Li, K. Zhang, K. Xie, W. Wei, Y. Gao, M. Bai, Y. Gao, Q. Hou, C. Shen, Z. Xia, B. Wei, Adv. Mater. 32 (2020) 1907079. <https://doi.org/10.1002/adma.201907079>.
- [59] Z. Hu, Z. Li, Z. Xia, T. Jiang, G. Wang, J. Sun, P. Sun, C. Yan, L. Zhang, Energy Storage Mater. 22 (2019) 29–39. <https://doi.org/10.1016/j.jensm.2018.12.020>.
- [60] R. Zhang, N. Wang, C. Shi, E. Liu, C. He, N. Zhao, Carbon 161 (2020) 198–205. <https://doi.org/10.1016/j.carbon.2020.01.077>.
- [61] H. Shi, J. Qin, K. Huang, P. Lu, C. Zhang, Y. Dong, M. Ye, Z. Liu, Z.-S. Wu, Angew. Chem. Int. Ed. 59 (2020) 12147–12153. <https://doi.org/10.1002/anie.202004284>.
- [62] C. Zhang, R. Lyu, W. Lv, H. Li, W. Jiang, J. Li, S. Gu, G. Zhou, Z. Huang, Y. Zhang, J. Wu, Q.-H. Yang, F. Kang, Adv. Mater. 31 (2019) 1904991. <https://doi.org/10.1002/adma.201904991>.
- [63] Y. Nan, S. Li, Y. Shi, S. Yang, B. Li, Small 15 (2019) 1903520. <https://doi.org/10.1002/smll.201903520>.
- [64] J. Li, P. Zou, S.W. Chi, W. Yang, P. Liu, C. Liang, F. Kang, C. Yang, Energy Storage Mater. 24 (2020) 700–706. <https://doi.org/10.1016/j.ensm.2019.06.019>.
- [65] L. Ye, M. Liao, H. Sun, Y. Yang, C. Tang, Y. Zhao, L. Wang, Y. Xu, L. Zhang, B. Wang, F. Xu, X. Sun, Y. Zhang, H. Dai, P.G. Bruce, H. Peng, Angew. Chem. Int. Ed. 58 (2019) 2437–2442. <https://doi.org/10.1002/anie.201814324>.
- [66] Z. Hu, H. Su, M. Zhou, J. Liu, Y. Wan, J. Hu, Y. Xu, Small 18 (2022) 2104735. <https://doi.org/10.1002/smll.202104735>.
- [67] J. Pu, J. Li, K. Zhang, T. Zhang, C. Li, H. Ma, J. Zhu, P.V. Braun, J. Lu, H. Zhang, Nat. Commun. 10 (2019) 1896. <https://doi.org/10.1038/s41467-019-09932-1>.
- [68] F. Ren, Z. Lu, H. Zhang, L. Huai, X. Chen, S. Wu, Z. Peng, D. Wang, J. Ye, Adv. Funct. Mater. 28 (2018) 1805638. <https://doi.org/10.1002/adfm.201805638>.
- [69] G. Yang, J. Chen, P. Xiao, P.O. Agboola, I. Shakir, Y. Xu, J. Mater. Chem. A 6 (2018) 9899–9905. <https://doi.org/10.1039/C8TA02810A>.
- [70] H. Mao, W. Yu, Z. Cai, G. Liu, L. Liu, R. Wen, Y. Su, H. Kou, K. Xi, B. Li, H. Zhao, X. Da, H. Wu, W. Yan, S. Ding, Angew. Chem. Int. Ed. 60 (2021) 19306–19313. <https://doi.org/10.1002/anie.202105831>.
- [71] N. Zhang, L. Du, J. Zhang, H. Xu, X. Zhou, L. Mai, L. Xu, Adv. Funct. Mater. 33 (2023) 2210862. <https://doi.org/10.1002/adfm.202210862>.
- [72] Y.-S. Feng, Y.-N. Li, P. Wang, Z.-P. Guo, F.-F. Cao, H. Ye, Angew. Chem. Int. Ed. 62 (2023) e202310132. <https://doi.org/10.1002/anie.202310132>.
- [73] J. Cao, Y. Xie, W. Li, X. Wang, Y. Yang, Q. Zhang, J. Guo, C. Yang, S. Cheng, C. Zhang, K. Wang, Mater. Today Energy 20 (2021) 100663. <https://doi.org/10.1016/j.mtener.2021.100663>.
- [74] H. Wang, J. Wu, L. Yuan, Z. Li, Y. Huang, ACS Appl. Mater. Interfaces 12 (2020) 28337–28344. <https://doi.org/10.1021/acsami.0c08029>.
- [75] F. Cheng, X. Yang, O. Ka, L. Wen, X. Wang, W. Lu, J. Mater. Chem. A 11 (2023) 4205–4219. <https://doi.org/10.1039/D2TA09182H>.

- [76] H. Ye, Z.-J. Zheng, H.-R. Yao, S.-C. Liu, T.-T. Zuo, X.-W. Wu, Y.-X. Yin, N.-W. Li, J.-J. Gu, F.-F. Cao, Y.-G. Guo, *Angew. Chem. Int. Ed.* 58 (2019) 1094–1099. <https://doi.org/10.1002/anie.201811955>.
- [77] D.W. Kang, S.S. Park, H.J. Choi, J.-H. Park, J.H. Lee, S.-M. Lee, J.-H. Choi, J. Moon, B.G. Kim, *ACS Nano* 16 (2022) 11892–11901. <https://doi.org/10.1021/acsnano.2c01309>.
- [78] A. Huang, H. Huang, S. Li, X. Pan, A.-Y. Wang, H.-Y. Chen, T. Wang, L. Li, M. Maximov, J. Ren, Y. Wu, S. Peng, *Adv. Energy Mater.* 15 (2025) 2403576. <https://doi.org/10.1002/aenm.202403576>.
- [79] S. Fan, Z. Sun, C. Liu, F. Ye, M. Liu, *ChemSusChem* 18 (2025) e202402472. <https://doi.org/10.1002/csc.202402472>.
- [80] Z. Hou, Y. Yu, W. Wang, X. Zhao, Q. Di, Q. Chen, W. Chen, Y. Liu, Z. Quan, *ACS Appl. Mater. Interfaces* 11 (2019) 8148–8154. <https://doi.org/10.1021/acsmami.9b01521>.
- [81] J.-P. Wang, D.-N. Lan, G.-Y. Chen, X.-T. Hu, C. Lin, Q. Li, *Small* 18 (2022) 2106718. <https://doi.org/10.1002/smll.202106718>.
- [82] J. Wang, S. Yao, R. Tao, X. Liu, J. Geng, C. Hong, H. Li, G. Yu, H. Li, X.-G. Sun, J. Li, J. Liang, *J. Energy Chem.* 97 (2024) 55–67. <https://doi.org/10.1016/j.jechem.2024.05.043>.
- [83] A. Pei, G. Zheng, F. Shi, Y. Li, Y. Cui, *Nano Lett.* 17 (2017) 1132–1139. <https://doi.org/10.1021/acs.nanolett.6b04755>.
- [84] K.-H. Chen, K.N. Wood, E. Kazak, W.S. LePage, A.L. Davis, A.J. Sanchez, N.P. Dasgupta, *J. Mater. Chem. A* 5 (2017) 11671–11681. <https://doi.org/10.1039/C7TA00371D>.
- [85] J.B. Park, C. Choi, S. Yu, K.Y. Chung, D.-W. Kim, *Adv. Energy Mater.* 11 (2021) 2101544. <https://doi.org/10.1002/aenm.202101544>.
- [86] G.-W. Lee, Y.J. Choi, Y.-H. Kim, S.-G. Choi, H.-S. Choi, H.-K. Kim, K.-B. Kim, *Carbon* 198 (2022) 289–300. <https://doi.org/10.1016/j.carbon.2022.07.048>.